WILEY | Hindawi

Research Article

Effect of Bedding Structure on the Energy Dissipation Characteristics of Dynamic Tensile Fracture for Water-Saturated Coal

Shuang Gong [1,2,3] **Lei Zhou** [1,2,3] **Zhen Wang,**[1,2,3] **and Wen Wang**[1,3]

[1]*School of Energy Science and Engineering, Henan Polytechnic University, Jiaozuo 454000, China*
[2]*Henan Key Laboratory for Green and Efficient Mining & Comprehensive Utilization of Mineral Resources, Jiaozuo 454000, China*
[3]*Collaborative Innovation Center of Coal Work Safety, Jiaozuo, 454000 Henan Province, China*

Correspondence should be addressed to Shuang Gong; gongcumtb@126.com

The analysis of energy dissipation characteristics is a basic way to elucidate the mechanism of coal rock fragmentation. In order to study the energy dissipation patterns during dynamic tensile deformation damage of coal samples, the Brazilian disc (BD) splitting test under impact conditions was conducted on burst-prone coal samples using a split Hopkinson pressure bar (SHPB) loading system. The effects of impact velocity, bedding angle, and water saturated on the total absorbed energy density, total dissipated energy density, and damage variables of coal samples were investigated. In addition, the coal samples were collected after crushing to produce debris with particle sizes of 0-0.2 mm and 0.2-5 mm, and the distribution characteristics of different size debris were compared and analyzed. The results show that the damage variables of natural dry coal samples increase approximately linearly with the increase of impact velocity; however, the overall damage variables of saturated coal samples increase exponentially as a function of impact velocity. Compared with air-dry samples, the number of fragments with the particle size of 0-0.2 mm of saturated samples decreases by 14.1%-31.3%, and the number of fragments with the particle size of 0.2-5 mm decreases by 33.7%-53.0%. However, when the bedding angle is 45°, the percentage of fragment mass of saturated samples is larger than that of air-dry samples. The conclusions provide a theoretical basis for understanding the deterioration mechanism of coal after water saturation and the implementation of water injection dust prevention technology in coal mines.

1. Introduction

Coal is China's basic energy and fuel resource, accounting for 59.0% of the total energy consumption in 2019. The energy dissipation law and fragment distribution characteristics of coal in the dynamic tensile failure are directly related to the blasting scheme, coal roadway support, hazard prevention measures of rock burst, and gas outburst in top coal caving mining [1]. Energy is the essential characteristic of physical reaction and the internal factor of substance failure through the whole deformation and failure process of coal rock. Therefore, the energy dissipation can be analyzed to clarify the crushing mechanism of coal rock [2–7]. However, compared with the total input energy, the effective energy for rock crushing is quite low in mining techniques such as percus-

sion drilling, blasting, and cutting. For example, during the cutting and drilling, only about 10% of the input energy is used for the effective crushing, while most of the input energy is dissipated in heat or other forms [8]; during the blasting, the energy utilization rate for rock crushing is only about 5%-15% [9]. Chi et al. concluded that less than 1% of the input energy is used to crush rock and form a new fracture surface [10]. Therefore, further quantitative study on the energy dissipation law and fragment distribution characteristics of coal samples under dynamic tensile failure are of great significance for the dynamic disaster prevention, resource recovery rate, and energy efficiency in coal mines.

Up to now, many scholars have studied the deformation and failure process of rock from the perspective of energy and have achieved sound results [11–16]. Song et al. [17]

(a)   (b)
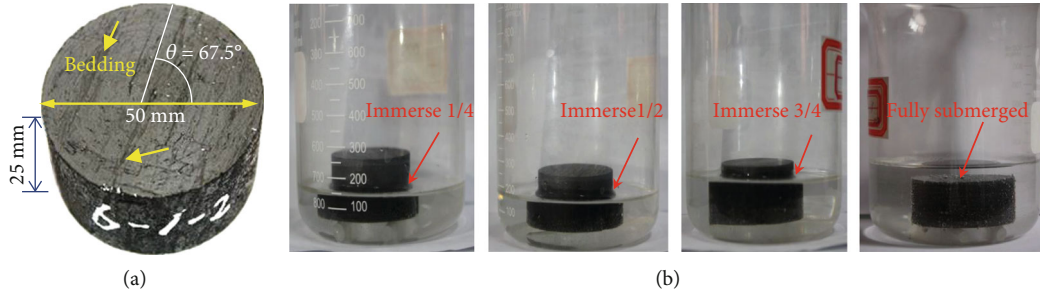
FIGURE 1: Schematic diagram of sample size and sample preparation. (a) The size and bedding angle of coal sample. (b) Water absorption process of saturated coal sample.
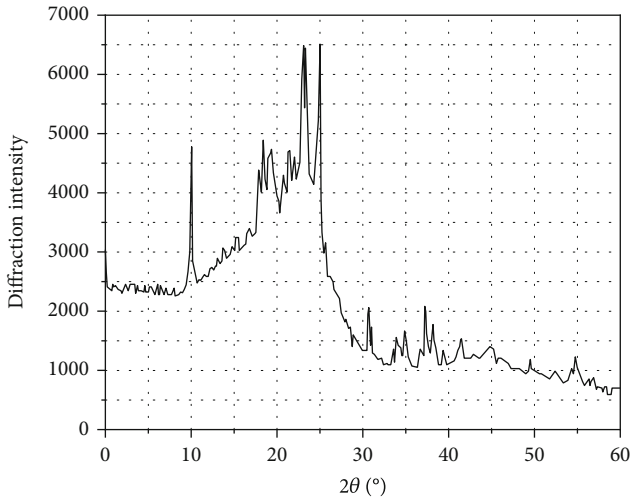

FIGURE 2: X-ray diffraction patterns of the coal specimen.

investigated the energy dissipation characteristics of concrete samples subjected to uniaxial cyclic loading based on the dissipated energy approach (DEA). The results show that the cumulative speed of energy dissipation and increasing growth rate of damage indicators in the continuum damage theory (CDT) follow an exponential function in relation to the maximum cyclic load level and follow a logarithmic function in relation to the minimum cyclic load level. Zhang et al. [18] studied the energy dissipation characteristics of the coal subjected to multilevel-frequency cyclic loading. Two hysteresis indexes were proposed according to the stress-strain relation during cyclic loading to predict the fatigue failure of coal samples. In addition, a lot of research works have been carried out by scholars in studying the deterioration mechanism of water on rocks. Cai et al. [19] investigate the effect of wetting-drying cycles on the fracture behavior of sandstone. Tests results indicate that both of fracture toughness and energy dissipation of sandstone significantly decrease with the increase of cycle number. Song et al. [20] studied the mechanical behavior of Tibet marble exposed to various freeze-thaw (FT) cycles and multilevel cyclic loading. A warning level is defined according to the evolution of radial strain and Poisson's ratio which can inform before dilation starts. The understanding of the energy dissipation characteristics of rock crushing is enhanced, and the development of mining technology is promoted. However, there are few

reports on the energy dissipation law of coal rock in the process of deformation and failure. Besides, the coal contains a certain amount of original moisture, bedding, and other primary structures, which increases the discreteness of dynamic tensile test results of coal rock [21]. Therefore, it is necessary to study the influence of bedding and water content on the energy dissipation characteristics of coal rock.

In this paper, the dynamic Brazilian splitting test was used to analyze the energy dissipation law of coal samples, and 90 disk-shaped coal samples were used for the SHPB impact splitting test. The effects of impact velocity, bedding angle, and saturated water content on the total absorbed energy density, total dissipated energy, total dissipated energy density, and damage variable of coal samples were discussed, and the distribution characteristics of the generated fragments with different sizes during the dynamic splitting of coal samples were compared and analyzed.

2. Experimental Setup

2.1. Sample Preparation. The coal samples were taken from the coal seam 11, panel 2, working face 8935 in Xinzhouyao mine, Datong, Shanxi Province. The coal was gathered from the Jurassic coal seam. To ensure the homogeneity of physical and mechanical properties of samples, all the samples were cut from a complete coal sample. A total of 90 coal samples with $\Phi 50\,mm \times 25\,mm$ was processed. The average diameter of coal samples was 49.29 mm, the average thickness was 25.27 mm, and the dimension error was ±1 mm. The unevenness of both ends after grinding was ±0.05 mm, and the end face was perpendicular to the axis. The maximum deviation was no more than 0.25°. The results showed that the uniaxial compressive strength, tensile strength, cohesion, internal friction angle, elastic modulus, and Poisson's ratio of coal samples were 27.64 MPa, 1.75 MPa, 7.85 MPa, 32.64°, 2.29 GPa, and 0.24, respectively. Through the proximate analysis of coal rock, the moisture content, ash content, and fixed carbon content of coal samples were 4.13%, 2.04%, and 69.17%, respectively.

As shown in Figure 1, a total of 90 Brazilian disc coal samples were finally processed, of which 45 coal samples were in the state of air-dry, and the remaining 45 coal samples were soaked in water for 161 hours to reach the state of saturated water content. According to the bedding angle (the angle between bedding plane and impact direction),

TABLE 1: Quantitative statistical results of coal samples' macerals.

Desmocollinites	Telocollinite	Telinite	Corpocollin-ite	Semifusinite	Fusinite	Inert detritus	Mineral
2.1	46.3	20.5	1.5	10.8	8.2	4.6	6.0

TABLE 2: Changes in parameters before and after saturation of coal samples.

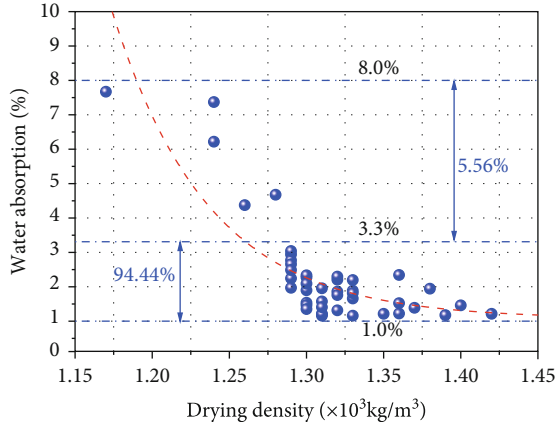| Specimen ID	Diameter (mm)	Height (mm)	Mass (dry) (g)	Drying density ($\times 10^3$kg/m^3)	Mass (saturated) (g)	Water absorption (%)
5-1-1	50.08	25.12	64.28	1.30	65.01	1.136
5-2-2	50.30	25.10	69.79	1.40	70.68	1.275
5-3-1	48.84	25.50	59.15	1.24	63.51	7.371
6-7-3	48.56	25.06	57.43	1.24	60.78	5.833
6-2-1	47.96	25.20	58.26	1.28	59.8	2.643

FIGURE 3: Relationship between saturated water absorption and density of coal sample.

the air-dry samples and saturated samples were divided into 5 groups (0°, 22.5°, 45°, 67.5°, and 90°). The results of X-ray diffraction (XRD) and maceral analysis of coal samples are shown in Figure 2 and Table 1, respectively. The changes of physical parameters of coal samples before and after water saturation are shown in Table 2. The water imbibition of 45 saturated samples was 1.2%-2.4%. Figure 3 shows the relationship between the water absorption of coal sample and its dry density. It can be concluded that 94.44% of the coal samples are in the water absorption rate of 1%~3.3%, and the distribution is relatively concentrated. Only 5.56% of the coal samples have water absorption of 3.3%~8.0%, and the distribution is relatively dispersed. Water absorption indirectly reflects the porosity of coal sample.

2.2. Split Hopkinson Pressure Bar (SHPB) Apparatus. The dynamic impact Brazilian splitting test of coal rock was carried out on the SHPB system (Figure 4). In the SHPB device, the diameter of the steel cylindrical bullet, the input rod, and the output rod were 50 mm, and the length of the steel cylindrical bullet, the input rod, and the output rod were 400 mm, 2000 mm, and 2000 mm, respectively. Strain gages were pasted at 1 m from the input rod and the output rod to the

end of the sample to record the rod strain. The muzzle velocity of the bullet was controlled by the air pressure in the air chamber, and the input rod velocity was measured by the photoelectric method.

2.3. Data Processing Method. The Hopkinson bar technique is based on the one-dimensional assumption and stress uniformity assumption. According to the stress uniformity assumption, the dynamic stress-strain relationship of the material is obtained by using the three-wave method [12]:

$$\left.\begin{array}{l} \dot{\varepsilon}(t) = \dfrac{c}{l_s}(\varepsilon_i - \varepsilon_r - \varepsilon_t) \\[2mm] \varepsilon(t) = \dfrac{c}{l_s}\displaystyle\int_0^t (\varepsilon_i - \varepsilon_r - \varepsilon_t)dt \\[2mm] \sigma(t) = \dfrac{A}{2A_s}E(\varepsilon_i + \varepsilon_r + \varepsilon_t) \end{array}\right\}, \tag{1}$$

where E, c, and A are the elastic modulus, elastic wave velocity, and cross-sectional area of the compression bar; A_s and l_s are the initial cross-sectional area and initial length of the sample; and ε_i, ε_r, and ε_t are the incident strain, reflected strain, and transmitted strain in the bar, respectively.

From loading to unloading, the energy carried by the incident wave, reflected wave, and transmitted wave are W_i, W_r, and W_t, respectively. The total dissipated energy of the sample is W_d, and the total dissipated energy density is w_d. The calculation equation is as follows [11, 12]:

$$\left.\begin{array}{l} W_i = \dfrac{AC_b}{E_b}\displaystyle\int \sigma_i^2 dt = AE_bC_b\displaystyle\int \varepsilon_i^2 dt \\[2mm] W_r = \dfrac{AC_b}{E_b}\displaystyle\int \sigma_r^2 dt = AE_bC_b\displaystyle\int \varepsilon_r^2 dt \\[2mm] W_t = \dfrac{AC_{bt}}{E_{bt}}\displaystyle\int \sigma_t^2 dt = AE_{bt}C_{bt}\displaystyle\int \varepsilon_t^2 dt \end{array}\right\}, \tag{2}$$

$$W_d = W_i - W_r - W_t, \tag{3}$$

$$w_d = \dfrac{W_d}{V}, \tag{4}$$
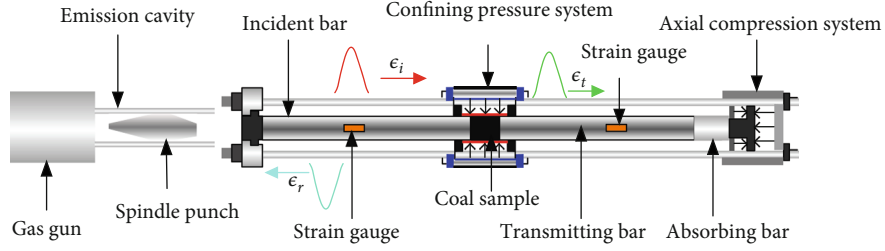
FIGURE 4: The Hopkinson pressure bar apparatus.

where σ_i, σ_r, and σ_t are the stresses of the incident wave, reflected wave, and transmitted wave on the pressure bar; V is the volume of the sample; C_b and C_{bt} are the propagation velocity of the sound wave in the input rod and output rod; and E_b and E_{bt} are elastic modulus of the input rod and output rod, respectively.

3. Results and Discussion

3.1. Definition of Damage Variable Based on Energy Dissipation. The split Hopkinson pressure bar test is based on one-dimensional elastic stress wave hypothesis and uniformity hypothesis. The stress-strain response characteristics of the sample are mainly reflected by the changes of the incident wave, reflected wave, and transmitted wave during the test. When the stress wave passes through the sample, the energy carried by the stress wave gradually decreases due to the existence of bedding and the formation and expansion of cracks in the sample. The energy carried by the incident wave minus the energy carried by the reflected wave and the transmitted wave is the energy consumed by the dynamic loading failure of the sample.

The research of damage can be based on two methods: micromechanics and macro phenomenology. In macroscopic phenomenology, different damage variables such as area, modulus, and energy can be defined. Li et al. [11] carried out dynamic SHPB impact test on sandstone samples and obtained the damage variables of sandstone samples under different impact velocities. Based on the understanding of constitutive energy and dissipated energy in material deformation, Jin et al. [15] defined the damage variable of material from the angle of energy dissipation, gave the theoretical formula of damage variable, and calculated the dissipated energy according to cyclic loading. Referring to the previous research, the damage variable d of dynamic impact tensile failure of coal sample is defined as follows:

$$d = \frac{w_d}{u}, \tag{5}$$

where u is the total absorbed energy density of the sample failure, i.e., the area enclosed by the stress-strain curve of coal samples.

$$u = \int \sigma d\varepsilon. \tag{6}$$

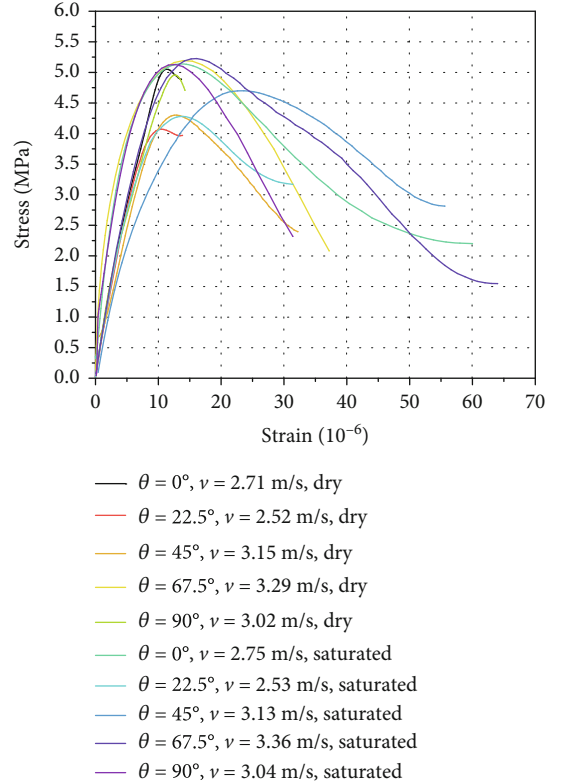Figure 5 shows the typical stress-strain curves of air-dry

FIGURE 5: The stress-strain curves of coal specimens with different bedding angles.

and saturated samples with different bedding angles. In the stress-strain curve of saturated samples, there is a long post-peak curve, indicating that saturated samples have large deformation. In contrast, air-dry samples have lower peak strength and smaller deformation before failure. The total absorbed energy density can be obtained by integrating the corresponding stress-strain curves.

Figure 6 shows the dynamic tensile strength of coal samples with different bedding angles before and after water saturation. It can be concluded that when the bedding plane is perpendicular or parallel to the incident direction (that is, the bedding angle is 0 or 90 degrees), the test results before and after water absorption are more concentrated and less discrete than those of other groups. In addition, the change of tensile strength of coal sample before and after water absorption has no fixed trend, which may be higher or lower than that of natural coal
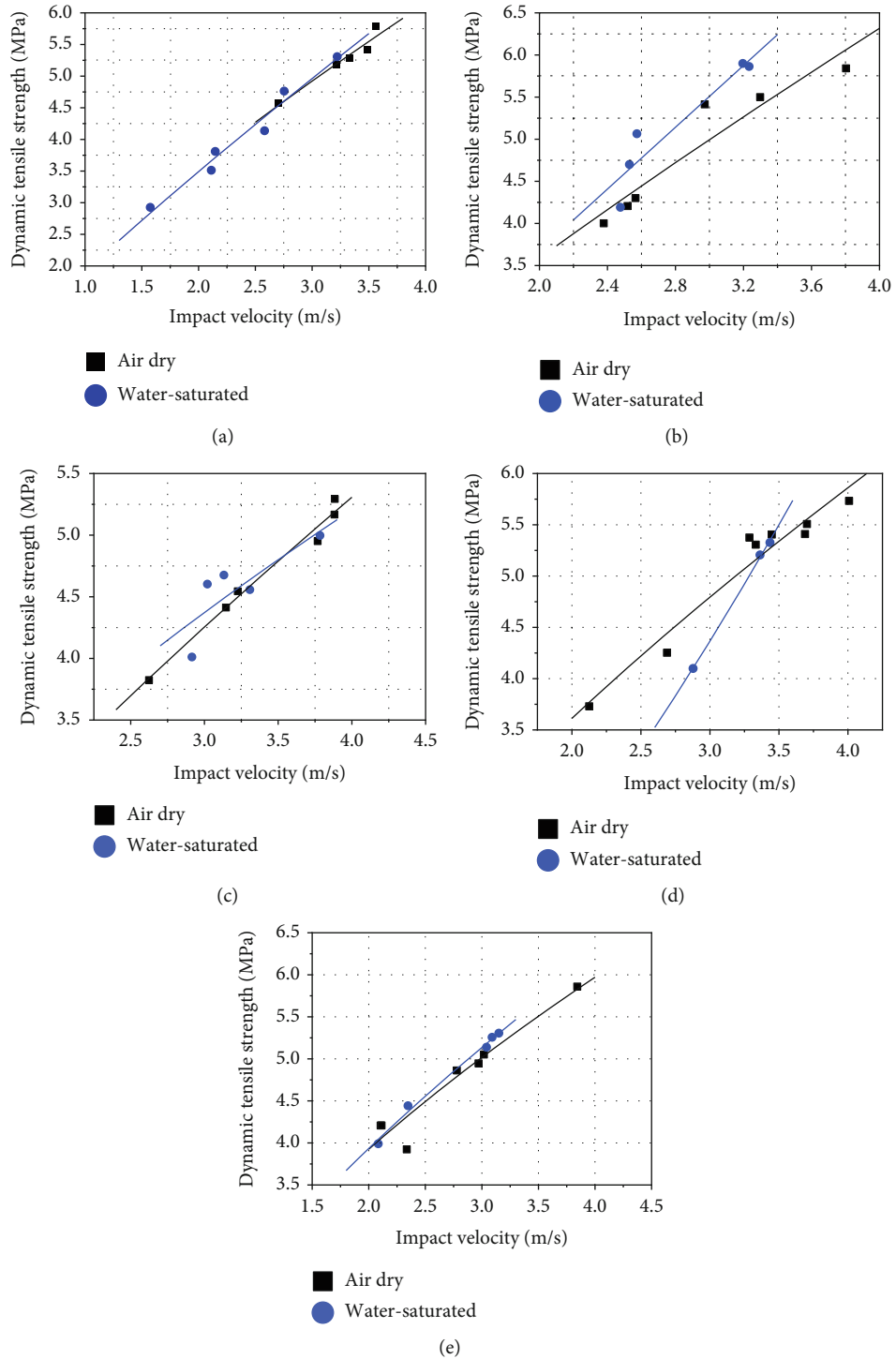
FIGURE 6: Comparison of relationship between dynamic tensile strength and impact velocity of coal rock specimens in natural state and water-saturated state. (a) $\theta = 0°$. (b) $\theta = 22.5°$. (c) $\theta = 45°$. (d) $\theta = 67.5°$. (e) $\theta = 90°$.

sample. This is determined by bedding angle and water absorption factors at the same time.

3.2. Energy Dissipation Law of Coal Samples. To analyze the influence of the total absorbed energy density, total dissipated energy density, total dissipated energy density, and damage variables on the response characteristics of different impact velocities, bedding angles, and saturated water con-

tents of coal samples, the energy dissipation characteristic parameters of 41 samples were successfully obtained, as shown in Table 3. It is found that under the similar impact velocity, the total absorbed energy density of air-dry samples is the largest at a bedding angle of 45° and the smallest at a bedding angle of 90°; the discreteness of coal samples with bedding angle of 0° is the largest and the discreteness of coal samples with a bedding angle of 22.5° is the smallest. For

TABLE 3: Energy dissipation parameters of air-dry and water-saturated coal specimens.

Water content	θ (°)	v (m·s^{-1})	u (J·m^{-3})	W_d (J)	w_d (J·m^{-3})	d
Dry	0	3.213	8137.23	0.042	863.16	0.1061
		2.695	2932.36	0.011	229.32	0.0782
		3.565	8588.66	0.045	914.02	0.1064
		2.707	2242.11	0.009	184.26	0.0822
	22.5	2.378	3689.26	0.012	246.45	0.0668
		2.518	5781.86	0.024	499.22	0.0863
		2.565	4790.71	0.016	338.42	0.0706
		2.972	5609.13	0.025	509.45	0.0908
	45	3.803	6916.84	0.038	768.85	0.1112
		2.624	4796.75	0.017	355.85	0.0742
		3.146	7126.37	0.039	788.59	0.1107
		3.226	7496.42	0.040	813.23	0.1085
	67.5	3.286	3465.82	0.018	385.75	0.1113
		4.008	6885.24	0.038	795.93	0.1156
		3.332	3573.23	0.021	438.17	0.1226
		2.125	5712.75	0.023	461.78	0.0808
	90	2.689	5387.65	0.022	465.73	0.0887
		3.843	7132.59	0.041	838.88	0.1176
		2.97	2970.66	0.013	265.34	0.0893
		2.779	8090.98	0.036	747.61	0.0924
		3.018	2273.96	0.010	207.83	0.0914
		2.336	1966.50	0.007	139.82	0.0711
Saturated	0	2.112	2684.75	0.009	190.35	0.0709
		1.58	3365.76	0.011	226.52	0.0673
		3.221	5051.66	0.026	542.48	0.1074
		2.754	5276.99	0.021	438.16	0.0831
	22.5	2.851	4614.83	0.019	450.41	0.0850
		2.529	10055.36	0.044	907.12	0.0902
		3.233	8140.09	0.029	598.02	0.0735
		2.573	9821.71	0.044	891.06	0.0907
	45	2.476	4127.82	0.016	321.21	0.0778
		3.132	9910.17	0.055	1141.26	0.1152
		3.308	9611.25	0.058	1217.89	0.1267
		2.915	5429.54	0.029	597.93	0.1101
	67.5	3.363	7578.40	0.047	990.95	0.1308
		3.435	3472.94	0.026	545.56	0.1571
		2.878	7965.75	0.035	713.34	0.0896
		3.041	9484.67	0.048	997.61	0.1052
	90	3.09	3600.11	0.019	398.34	0.1106
		2.347	5490.83	0.021	450.85	0.0821
		2.084	3723.11	0.013	281.84	0.0751

Note: θ: bedding angle; v: impact velocity; u: density of total absorbed energy; W_d: total dissipated energy; w_d: density of total dissipated energy; d: damage variables.

saturated samples, the total absorbed energy density and discreteness are the smallest at a bedding angle of 0°, the total absorbed energy density is the largest at a bedding angle of 45°, and the discreteness is the largest at a bedding angle of 90°. The results show that the total dissipated energy density of air-dry coal sample is the highest at the bedding angle of 45° and the lowest at a bedding angle of 90°; the total dissipated energy density of saturated samples is the highest at a bedding angle of 45° and the lowest at a bedding angle of 0°.

The fitting relationship between damage variables of coal samples with different bedding angles and impact loading velocity under air-dry and saturated conditions is shown in
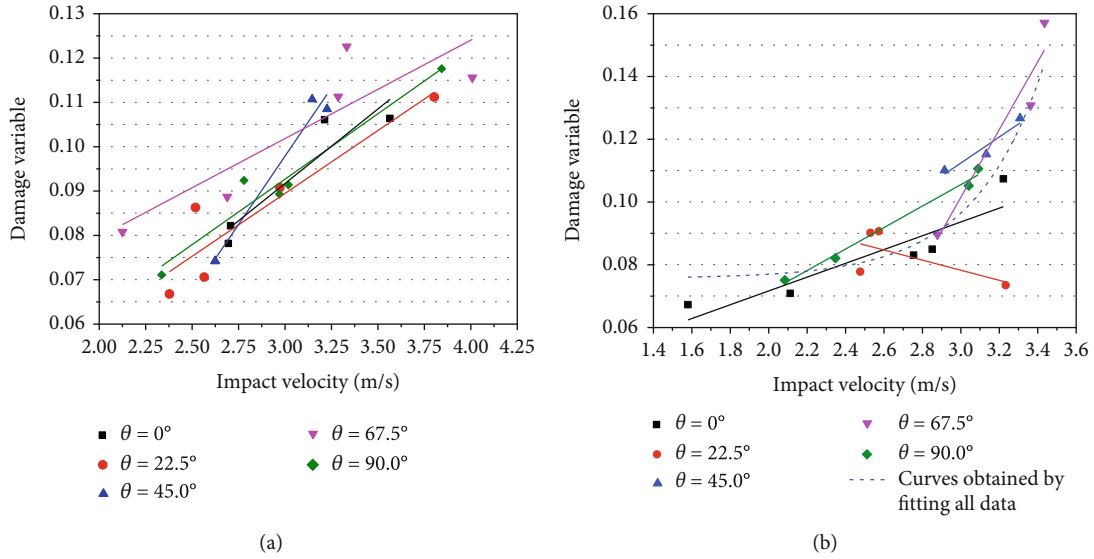
(a)

(b)

FIGURE 7: Relationship between damage variable and impact velocity of coal samples.
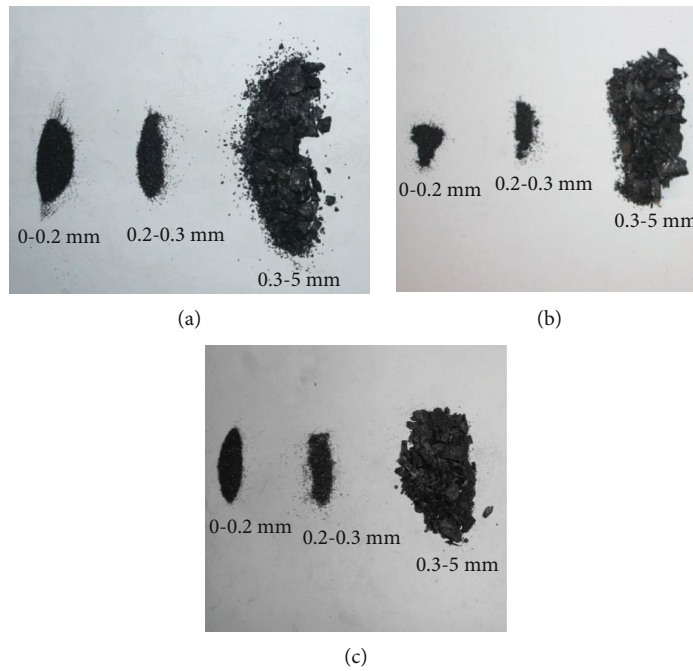

(a)

(b)

(c)

FIGURE 8: Size statistics of fragments of coal with different bedding angles under the impact loading. From (a) to (c), the bedding angle is 0°, 45°, and 90°, respectively.

Equations (7) and (8)

$$
\begin{cases}
d_1 = -0.00915 + 0.03362v & (\theta = 0°), \\
d_1 = 0.00436 + 0.02837v & (\theta = 22.5°), \\
d_1 = -0.08702 + 0.06163v & (\theta = 45.0°), \\
d_1 = 0.03525 + 0.0222v & (\theta = 67.5°), \\
d_1 = 0.00411 + 0.02952v & (\theta = 90.0°),
\end{cases} \tag{7}
$$

$$
\begin{cases}
d_2 = 0.02771 + 0.02198v & (\theta = 0°), \\
d_2 = 0.12654 - 0.01609v & (\theta = 22.5°), \\
d_2 = -0.01215 + 0.04152v & (\theta = 45.0°), \\
d_2 = -0.22251 + 0.108v & (\theta = 67.5°), \\
d_2 = 0.00286 + 0.03423v & (\theta = 90.0°).
\end{cases} \tag{8}
$$

Figures 7(a) and 7(b) show the relationship between damage variable and impact velocity of air-dry and water-
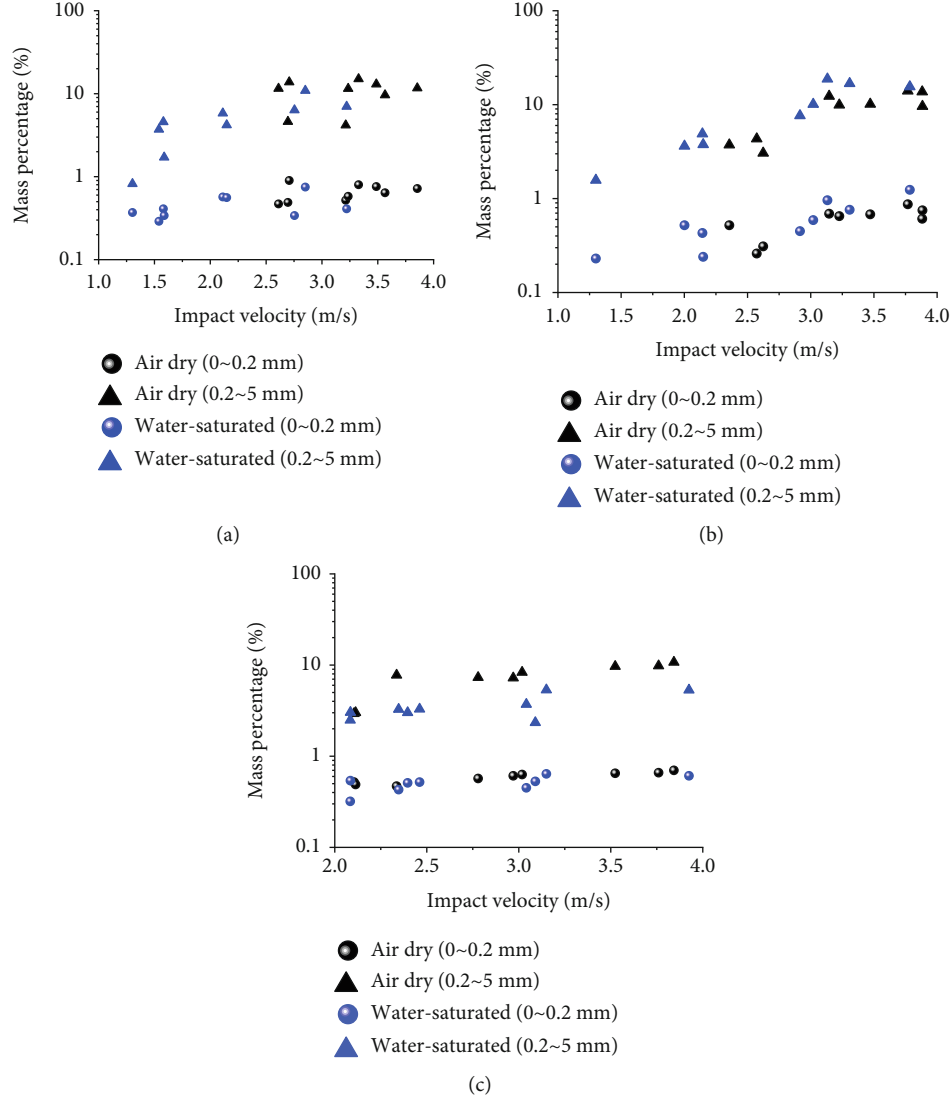
(a)

(b)

(c)

FIGURE 9: Size distribution of fragments of air-dry coal and water-saturated coal specimens after failure under the dynamic impact loading. From (a) to (c), the bedding angle is 0°, 45°, and 90°, respectively.

TABLE 4: Statistics of the average value of debris of two particle sizes for dry and water-saturated coal samples after impact loading.

θ	(0~0.2 mm, dry, W_{d1})	(0.2~5 mm, dry, W_{d2})	(0~0.2 mm, saturated, W_{w1})	(0.2~5 mm, saturated, W_{w2})	$(W_{d1} - W_{w1})/W_{d1}$ (%)	$(W_{d2} - W_{w2})/W_{d2}$ (%)
0°	0.653	10.551	0.4489	5.007	31.2557	52.54478
22.5°	0.617	9.004	0.4878	5.968	20.94003	33.71835
45°	0.593	8.97	0.602	9.183	-1.517707	-2.3746
67.5°	0.776	11.879	0.54	5.579	30.41237	53.03477
90°	0.589	7.4189	0.506	3.533	14.09168	52.37838

saturated samples. When the impact velocity is 2.0-4.25 m/s, the damage variable of air-dry coal sample is in the range of 0.06-0.13; when the impact velocity is 1.5-3.6 m/s, the damage variable of saturated samples is in the range of 0.06-0.16. Therefore, the damage variables of air-dry and saturated samples with the same bedding angle increase approximately linearly with the increase of impact velocity. When the

impact velocity is less than 3.1 m/s, the damage variable of air-dry samples with a bedding angle of 67.5° is the largest; when the impact velocity is greater than 3.1 m/s, the damage variable of air-dry samples with a bedding angle of 45.0° is the largest. The overall damage variable of saturated samples increases exponentially with impact velocity, and the fitting function is shown in Equation (9). However, for the saturated

samples with bedding angle of 22.5°, the overall damage variable shows a downward trend with the increase of the impact velocity, which may be caused by the increased heterogeneity of coal sample due to its full water content or the small number of successful samples.

$$d_2 = 5.692 \times 10^{-6} e^{v/0.3656} + 0.07565. \quad (9)$$

3.3. Fragment Distribution Characteristics. During the test, the generated fragments with particle sizes of 0-0.2 mm, 0.2-0.3 mm, and 0.3 mm-5 mm after the crushing of coal samples were collected and weighed. Figure 8 shows the particle size statistics of the fragments of coal samples with a bedding angle of 0°, 45°, and 90° under the impact velocity range of 1.58-3.882 m/s. With the increase of impact velocity, the number of fragments with the particle size of 0-0.2 mm and 0.2-0.3 mm increases after the failure of coal sample with the same bedding angle. This is because in the SHPB test, the greater the impact loading rate, the greater the energy carried by the incident wave, the greater the total dissipated energy density, and damage variable of the coal sample, and the more energy absorbed by the coal sample, the more fragments with the small size. The shape of fragments with the particle size of 0.3-5 mm is mainly flake, block, and granular.

Figures 9(a)–9(c) shows the fragment distribution with the particle size of 0 - 0.2 mm and 0.2-5 mm generated from air-dry samples and saturated samples with different bedding angles under dynamic impact loading. Since the distribution range of mass percentage of fragments with different particle sizes after crushing is large, a semilogarithmic coordinate is adopted in the figure to reflect its distribution characteristics. According to the scale characteristics of semilogarithmic coordinates, for fragments with the particle size of 0-0.2 mm generated from the air-dry and saturated samples, the percentage of fragment mass has little change with the increase of impact velocity (0.4489%-0.776%). However, for fragments with the particle size of 0.2-5 mm generated from the air-dry and saturated samples, the percentage of fragment mass increases significantly with the increase of impact velocity (3.533%-11.879%), and the percentage of fragments with the particle size of 0.2-5 mm generated from saturated samples is significantly less than that of air-dry samples under the same impact velocity. The previous research on the field dust prevention by the water injection [22–24] shows that the dust production in the water injection area is reduced by 38%-50%. This conclusion experimentally confirms the technical principle of water-injection dust-reduction technology in the mining process.

Table 4 shows the average value statistics of fragments with two particle sizes after impact loading on the air-dry and saturated samples. Compared with fragments generated from air-dry samples, the number of fragments with the particle size of 0-0.2 mm generated from saturated samples is reduced by 14.1%-31.3%, and the number of fragments with the particle size of 0.2-5 mm generated from saturated samples is reduced by 33.7%-53.0%. However, when the bedding angle is 45°, the percentage of fragment mass with the particle size of 0-0.2 mm and 0.2-5 mm generated from saturated samples is larger than that of air-dry samples. The reason

for this phenomenon needs to be further studied. However, previous field observations show that the effect of water-injection dust-prevention has a great relationship with the coal bedding, and the main joint system and the angle between the main joint system and the direction of working face in the longwall mining are the important factors [25].

4. Conclusions

(1) There is a long postpeak section in the stress-strain curves of saturated samples, which indicates the occurrence of the large deformation in saturated samples. In contrast, air-dry samples have lower peak strength and smaller deformation before failure

(2) The damage variable of coal samples under dynamic impact increases with the increase of impact velocity. And the overall damage variables of water-saturated coal samples increased exponentially with the increase of impact velocity

(3) For fragments with the particle size of 0-0.2 mm generated from air-dry and water-saturated samples, the percentage of fragment mass has little change with the increase of impact velocity. However, for fragments with the particle size of 0.2-5 mm generated from the air-dry and saturated samples, the percentage of fragment mass increases significantly with the increase of impact velocity, and the percentage of fragments with the particle size of 0.2-5 mm generated from saturated samples is significantly less than that of air-dry samples under the same impact velocity

(4) Compared with fragments generated from air-dry samples, the number of fragments with the particle size of 0-0.2 mm generated from saturated samples is reduced by 14.1%-31.3%, and the number of fragments with the particle size of 0.2-5 mm generated from saturated samples is reduced by 33.7%-53.0%. However, when the bedding angle is 45°, the percentage of fragment mass in saturated samples with the particle size of 0-0.2 mm and 0.2-5 mm is larger than that in air-dry samples

Data Availability

The data used to support the findings of this study are available from the corresponding author upon request.

Conflicts of Interest

The authors declare that they have no conflicts of interest.

Acknowledgments

References

[1] S. Gong, *Study on Mechanical Characteristics of Dynamic Tensile and Mode I Fracture of Coal Samples under Impact Loading*, China University of Mining and Technology, Beijing, 2018.

[2] L. Yuan and P. S. Zhang, "Development status and prospect of geological guarantee technology for precise coal mining," *Journal of China Coal Society*, vol. 44, no. 8, pp. 2277–2284, 2019.

[3] W. Cai, L. Dou, G. Si et al., "A new seismic-based strain energy methodology for coal burst forecasting in underground coal mines," *International Journal of Rock Mechanics and Mining Sciences*, vol. 123, p. 104086, 2019.

[4] A. Mottahedi and M. Ataei, "Fuzzy fault tree analysis for coal burst occurrence probability in underground coal mining," *Tunnelling and Underground Space Technology*, vol. 83, pp. 165–174, 2019.

[5] D. Song, X. He, E. Wang, Z. Li, M. Wei, and H. Mu, "A dynamic ejection coal burst model for coalmine roadway collapse," *International Journal of Rock Mechanics and Mining Sciences*, vol. 29, no. 4, pp. 557–564, 2019.

[6] I. Anthony and T. Stephen, "Occurrence, predication, and control of coal burst events in the U.S," *International Journal of Mining Science and Technology*, vol. 26, no. 1, pp. 39–46, 2016.

[7] X. W. Li and Y. J. Chai, "Determination of pillar width to improve mining safety in a deep burst-prone coal mine," *Safety Science*, vol. 113, pp. 244–256, 2019.

[8] M. M. Carroll, "Mechanics of geological materials," *Applied Mechanics Division*, vol. 70, no. 38, pp. 1256–1260, 1985.

[9] V. I. Revnintsev, "We really need revolution in comminution," in *XVI International Mineral Processing Congress*, pp. 93–114, Elsevier Science Publishers, Amsterdam, 1988.

[10] G. Chi, M. C. Fuerstenau, R. C. Bradt, and A. Ghosh, "Improved comminution efficiency through controlled blasting during mining," *International Journal of Mineral Processing*, vol. 47, no. 1-2, pp. 93–101, 1996.

[11] L. Y. Li, Z. J. Xu, H. P. Xie, Y. Ju, X. Ma, and Z. C. Han, "Failure experimental study on energy laws of rock under differential dynamic impact velocity," *Journal of China Coal Society*, vol. 36, no. 12, pp. 2007–2011, 2011.

[12] J. Y. Xu and S. Liu, "Analysis of engrgy dissipation rule during deformation and fracture process of rock under high temperatures in SHPB test," *Chinese Journal of Rock Mechanics and Engineering*, vol. 32, no. S2, pp. 3109–3115, 2013.

[13] B. Bohloli and E. Hoven, "A laboratory and full-scale study on the fragmentation behavior of rocks," *Engineering Geology*, vol. 89, no. 1-2, pp. 1–8, 2007.

[14] A. Hua, Y. Kong, S. Li, and Y. Li, "Energy analysis of depressurized rock fracture," *Journal of China Coal Society*, vol. 4, pp. 389–392, 1995.

[15] F. N. Jin, M. R. Jiang, and X. L. Gao, "Defining damage variable based on energy dissipation," *Chinese Journal of Rock Mechanics and Engineering*, vol. 23, no. 12, pp. 1976–1980, 2004.

[16] Y. S. Zhao, Z. C. Feng, and Z. J. Wan, "Least energy principle of dynamical failure of rock mass," *Chinese Journal of Rock Mechanics and Engineering*, vol. 22, no. 11, pp. 1781–1783, 2003.

[17] Z. Y. Song, T. Frühwirt, and H. Konietzky, "Characteristics of dissipated energy of concrete subjected to cyclic loading," *Construction and Building Materials*, vol. 168, pp. 47–60, 2018.

[18] M. Zhang, L. Dou, H. Konietzky, Z. Song, and S. Huang, "Cyclic fatigue characteristics of strong burst-prone coal: experimental insights from energy dissipation, hysteresis and micro-seismicity," *International Journal of Fatigue*, vol. 133, p. 105429, 2020.

[19] X. Cai, Z. Zhou, L. Tan, H. Zang, and Z. Song, "Fracture behavior and damage mechanisms of sandstone subjected to wetting- drying cycles," *Engineering Fracture Mechanics*, vol. 234, p. 107109, 2020.

[20] Z. Song, Y. Wang, H. Konietzky, and X. Cai, "Mechanical behavior of marble exposed to freeze-thaw-fatigue loading," *International Journal of Rock Mechanics and Mining Sciences*, vol. 138, p. 104648, 2021.

[21] S. Gong, Z. Wang, L. Zhou, and W. Wang, "Influence of cyclic impact loading and axial stress on dynamic mechanical properties of burst-prone coal," *Shock and Vibration*, vol. 2021, Article ID 6649308, 10 pages, 2021.

[22] J. Cervik, A. Sainato, and E. Baker, *Water Infusion: An Effective and Economical Longwall Dust Control*, U.S. Department of the Interior, Bureau of Mines, Pittsburgh, PA, 1983.

[23] J. J. Mcclelland, *Water Infusion for Coal Mine Dust Control: Three Case Studies*, USBM Final Report, Pittsburgh, PA, 1987.

[24] G. A. Shirey, J. F. Colinet, and J. A. Kost, *Dust Control Handbook for Longwall Mining Operations*, USBM Final Report, Monroeville, PA, 1985.

[25] F. N. Kissell, *Information Circular 9465 Handbook for Dust Control in Mining*, U.S. Department of Health and Human Services, Public Health Service, Centers for Disease Control and Prevention, National Institute for Occupational Safety and Health, DHHS (NIOSH), Pittsburgh, PA, 2003.